

Article

SrTiO₃-SrVO₃ Ceramics for Solid Oxide Fuel Cell Anodes: A Route from Oxidized Precursors

Javier Macías[†], Jorge R. Frade and Aleksey A. Yaremchenko * 

CICECO—Aveiro Institute of Materials, Department of Materials and Ceramic Engineering, University of Aveiro, 3810-193 Aveiro, Portugal; javier.macias@bondalti.com (J.M.); jfrade@ua.pt (J.R.F.)

* Correspondence: ayaremchenko@ua.pt

[†] Current address: Bondalti, Rua do Amoníaco Português 10, 3860-680 Estarreja, Portugal.

Abstract: Perovskite-type Sr(Ti,V)O_{3-δ} ceramics are promising anode materials for natural gas- and biogas-fueled solid oxide fuel cells, but the instability of these phases under oxidizing conditions complicates their practical application. The present work explores approaches to the fabrication of strontium titanate-vanadate electrodes from oxidized precursors. Porous ceramics with the nominal composition SrTi_{1-y}V_yO_z ($y = 0.1-0.3$) were prepared in air via a solid state reaction route. Thermal processing at temperatures not exceeding 1100 °C yielded composite ceramics comprising perovskite-type SrTiO₃, pyrovanadate Sr₂V₂O₇ and orthovanadate Sr₃(VO₄)₂ phases, while increasing firing temperatures to 1250–1440 °C enabled the formation of SrTi_{1-y}V_yO₃ perovskites. Vanadium was found to substitute into the titanium sublattice predominantly as V⁴⁺, even under oxidizing conditions at elevated temperatures. Both perovskite and composite oxidized ceramics exhibit moderate thermal expansion coefficients in air, 11.1–12.1 ppm/K at 30–1000 °C, and insignificant dimensional changes induced by reduction in a 10%H₂-N₂ atmosphere. The electrical conductivity of reduced perovskite samples remains comparatively low, ~10⁻¹ S/cm at 900 °C, whereas the transformation of oxidized vanadate phases into high-conducting SrVO_{3-δ} perovskites upon reduction results in enhancement in conductivity, which reaches ~3 S/cm at 900 °C in porous composite ceramics with nominal composition SrTi_{0.7}V_{0.3}O_z. The electrical performance of the composite is expected to be further improved by optimization of the processing route and microstructure to facilitate the reduction of the oxidized precursor and attain better percolation of the SrVO₃ phase.



Citation: Macías, J.; Frade, J.R.; Yaremchenko, A.A. SrTiO₃-SrVO₃ Ceramics for Solid Oxide Fuel Cell Anodes: A Route from Oxidized Precursors. *Materials* **2023**, *16*, 7638. <https://doi.org/10.3390/ma16247638>

Academic Editor: Katsuhiko Ariga

Received: 20 November 2023

Revised: 10 December 2023

Accepted: 11 December 2023

Published: 14 December 2023



Copyright: © 2023 by the authors. Licensee MDPI, Basel, Switzerland. This article is an open access article distributed under the terms and conditions of the Creative Commons Attribution (CC BY) license (<https://creativecommons.org/licenses/by/4.0/>).

Keywords: perovskite; titanate; vanadate; composite; SOFC; anode; electrical conductivity

1. Introduction

Oxide phases derived from perovskite-type SrTiO₃ and SrVO₃ are considered potential alternatives to traditional Ni-YSZ (yttria-stabilized zirconia) anode materials used in hydrocarbon-fueled solid oxide fuel cells (SOFCs) [1–6]. Apart from issues related to redox instability and microstructural degradation due to the agglomeration of nickel particles with time [7,8], Ni-YSZ cermets suffer from coking and poisoning by ppm levels of H₂S contaminant in fuels such as natural gas or biogas [1,9]. In contrast, SrTiO₃- and SrVO₃-based ceramics are reported to exhibit good resistance to carbon deposition and tolerance towards sulfur poisoning [10–15].

Ceramic anode components based on SrTiO₃ and SrVO₃ have their pros and cons. The perovskite-type SrTiO₃ lattice exhibits remarkable redox and dimensional stability in a wide range of T-p(O₂) conditions [2,16], which is essential for SOFC anode applications. Although the electrical conductivity of SrTiO₃ under reducing conditions can be improved by donor-type substitutions into one or both sublattices, it remains moderate, ≤10 S/cm under typical anode operation conditions [17–20]. Furthermore, donor-doped strontium titanates prepared under oxidizing conditions demonstrate a long relaxation of electrical conductivity due to the slow reduction kinetics at SOFC operation temperatures [21–23]. The characteristics of SrVO_{3-δ} relevant to SOFC anode application are the

opposite. This perovskite exhibits high metallic-like electronic conductivity under reducing conditions, ~ 1000 S/cm at 800 °C [24–26], and non-negligible oxygen deficiency in the lattice [26,27], which may imply reasonable oxygen-ionic contribution to the total conductivity and is favorable for electrochemical performance. At the same time, undoped $\text{SrVO}_{3-\delta}$ ceramics have an excessive thermal expansion coefficient (TEC, average 18–19 ppm/K at 100–1000 °C [26,28]) that complicates their thermomechanical compatibility with other SOFC components. Also, perovskite-like $\text{SrVO}_{3-\delta}$ is stable only under reducing conditions below $p(\text{O}_2) \sim 10^{-15}$ and 10^{-17} atm at 900 and 800 °C, respectively [24,26,29]. To some extent, the stability domain of the perovskite phase can be expanded via suitable substitutions into strontium and/or vanadium sublattices [29,30].

SrTiO_3 and $\text{SrVO}_{3-\delta}$ form a continuous series of perovskite-like solid solutions under reducing conditions [28,31,32]. Balancing fractions of titanium and vanadium cations in the B sublattice enables a reasonable compromise between phase stability and the level of electrical conductivity and also allows one to adjust the thermochemical expansion [28,33]. In particular, $\text{SrTi}_{0.5}\text{V}_{0.5}\text{O}_{3-\delta}$ perovskite ceramics with intermediate titanium and vanadium content showed electrical conductivity of ~ 20 S/cm at 900 °C combined with a phase stability domain extended up to $p(\text{O}_2)$ of at least 10^{-11} atm at 900 °C and average TEC of 15 ppm/K [28]. The material still undergoes oxidative decomposition into titanium- and vanadium-rich phases when heated in air. The re-reduction does not recover the initial perovskite phase but may induce even slightly higher electrical conductivity compared to initial values [28].

Due to phase stability issues, $\text{Sr}(\text{Ti},\text{V})\text{O}_3$ -based anodes may be prepared either under reducing conditions or under an inert atmosphere where oxidation kinetics are sluggish [28,33]. However, from a practical point of view, it would be of interest to fabricate anodes of solid oxide cells under an ambient atmosphere (air) with a subsequent in-situ reduction, similar to what is practiced in the case of Ni-YSZ cermets. Therefore, the goal of the present study is to evaluate the possibility of preparing $\text{Sr}(\text{Ti},\text{V})\text{O}_3$ precursors under oxidizing conditions and to assess their redox behavior. The reported experimental studies of oxidized V-doped SrTiO_3 are mainly focused on the preparation of powdered samples with small vanadium additions (≤ 5 mol.%) at relatively low temperatures and their characterization for photocatalytic applications [34–37]. Park et al. [38] prepared mesoporous $\text{SrTi}_{0.8}\text{V}_{0.2}\text{O}_3$ thin films and studied their room-temperature thermoelectric properties. Mantry et al. [39] attempted the preparation of $\text{SrTi}_{1-x}\text{V}_x\text{O}_3$ ($x = 0.05\text{--}0.20$) ceramics via the solid state reaction method with sintering at 1250 °C and reported that all samples comprised phase impurities including $\text{Sr}_2\text{V}_2\text{O}_7$.

Two approaches to the oxidized $\text{Sr}(\text{Ti},\text{V})\text{O}_3$ precursors are comparatively explored in the present work: (i) synthesis of single-phase perovskite ceramics; and (ii) preparation of composites based on the SrTiO_3 and Sr-V-O phases. The studies are focused on ceramic samples with moderate vanadium additions (Ti:V ratio from 9:1 to 7:3) and porous microstructure (to simulate porous electrode layers of solid oxide cells) and include the characterization of phase composition, electrical conductivity, thermal expansion and the corresponding changes induced by reduction.

2. Materials and Methods

Materials with the nominal composition $\text{SrTi}_{1-y}\text{V}_y\text{O}_z$ (STV; $y = 0.1, 0.2, 0.3$) were prepared by solid state reaction route. SrCO_3 (purity > 99.9%, Sigma Aldrich, St. Louis, MO, USA), TiO_2 (>99.8%, Sigma Aldrich) and V_2O_5 (>99%, Fluka) were used as starting chemicals. The mixtures of reagents taken in appropriate proportions were preliminarily calcined in air at 500 °C/5 h and 600 °C/5 h, with intermediate regrinding, to promote the onset of Sr-V-O phases at temperatures below the melting point of V_2O_5 ($T_{\text{melt}} = 681$ °C). Then, the pre-calcined precursor mixtures were divided into two batches.

The first batch of each composition was calcined in air at 900–1100 °C, with a stepwise increase in temperature in increments of 50 °C, duration of 5 h at each step, and regrinding between the steps. Then, the powders were ball-milled with ethanol at 150 rpm for 4 h

using a Retsch S1 planetary mill (Retsch GmbH, Haan, Germany), nylon containers and Tosoh tetragonal zirconia balls. After milling and drying, the powders were compacted uniaxially into disk-shaped pellets and sintered in air at 1000 °C for 5 h. Hereafter, these samples are notated as STV-C or STV yy -C, where “C” stands for “composite” and “ yy ” indicates the percentage of vanadium cations in the B-sublattice.

The second batch of each composition was calcined in air in the regime of increasing calcination temperature stepwise, with steps of 40–100 °C and a duration of 5 h at each step, with regrinding between the steps, until X-ray diffraction (XRD) confirmed the absence of secondary phases. The highest calcination temperature was 1250, 1350 and 1440 °C for $y = 0.1, 0.2$ and 0.3 , respectively. After subsequent ball-milling and drying, disc-shaped pellets were compacted and sintered in air at 1100 °C for 5 h. These samples are referred to as STV-P or STV yy -P, where “P” indicates “perovskite”.

The sintered ceramic samples were polished using SiC grinding paper (Buehler, Leinfelden-Echterdingen, Germany). The density of the prepared ceramics was calculated using the geometric dimensions and mass of the polished samples. Rectangular bars for electrical and dilatometric measurements were cut out of the disk-shaped pellets using a Struers Minitom precision cutting machine (Struers, Copenhagen, Denmark) with a diamond cut-off wheel. Powdered samples for XRD studies and thermogravimetric analyses (TGAs) were prepared by grinding sintered ceramics in a mortar.

The XRD patterns of the powdered samples were recorded on a PANalytical X'Pert PRO diffractometer (PANalytical, Almelo, The Netherlands, CuK α radiation, step 0.026°) in the range $2\theta = 20$ –80°. The lattice parameters were calculated from the XRD data using FullProf software (profile matching method). Microstructural characterization was performed by scanning electron microscopy (SEM) using a Hitachi SU-70 microscope (Hitachi, Tokyo, Japan) equipped with a Bruker Quantax 400 detector (Bruker, Berlin, Germany) for energy dispersive spectroscopy (EDS) analysis. Thermogravimetric analysis (TGA, Setaram SetSys 16/18 instrument (Setaram, Caluire, France); sensitivity: 0.4 μ g; initial sample weight: ~0.5 g) was carried out on heating in a flowing 10% H_2 - N_2 mixture in the temperature range of 25–1000 °C with a constant rate of 2 °C/min followed by the isothermal step at 1000 °C. Dilatometric studies were conducted using a vertical alumina Linseis L70 dilatometer (Linseis, Selb, Germany) on heating/cooling at 3 °C/min in flowing air or a 10% H_2 - N_2 mixture.

Total electrical conductivity (σ) was determined employing AC impedance spectroscopy (2-probe method, Agilent 4284A precision LCR meter (Agilent, Santa Rosa, CA, USA); frequency range: 20 Hz–1 MHz; AC amplitude 1 V) and bar-shaped ceramic samples with porous Pt electrodes (Heraeus CL-11-5349 platinum paste, sintering at 1000 °C for 30 min) applied onto the end-faces of the bars. The measurements were performed in air in the temperature range of 750–1000 °C in a stepwise cooling regime. The relaxation of the electrical conductivity of samples on reduction was studied isothermally at 900 °C as a function of time on switching from an oxidizing (air) to a reducing atmosphere. A common procedure for the reduction of traditional Ni-YSZ cermet anodes during solid oxide cell start-up is purging with diluted hydrogen (e.g., 5–10 vol.% in nitrogen) [40,41]. A similar reducing atmosphere, a 10% H_2 - N_2 mixture, was employed in the present work.

The values of oxygen partial pressure $p(O_2)$ in the gas flow during the experiments were monitored employing homemade potentiometric YSZ sensors. The representative $p(O_2)$ value in the 10% H_2 - N_2 gas mixture corresponded to $\sim 10^{-20}$ atm at 900 °C.

3. Results and Discussion

3.1. Phase Composition, Structure and Microstructure of As-Prepared Samples

XRD analysis of the as-prepared STV-P samples confirmed the formation of a SrTiO $_3$ -based phase with a cubic perovskite structure (Figure 1A), without detectable phase impurities. All reflections in the XRD patterns were indexed in space group $Pm\bar{3}m$. The calculated lattice parameters decrease with increasing vanadium content in the perovskite lattice (Table 1), which is reasonable considering that the ionic radii of V $^{4+}$ and V $^{5+}$ cations

are smaller than that of Ti^{4+} [42]. This trend is also in agreement with data reported for the $\text{SrTi}_{1-y}\text{V}_y\text{O}_{3-\delta}$ series prepared under reducing conditions [28,31,32].

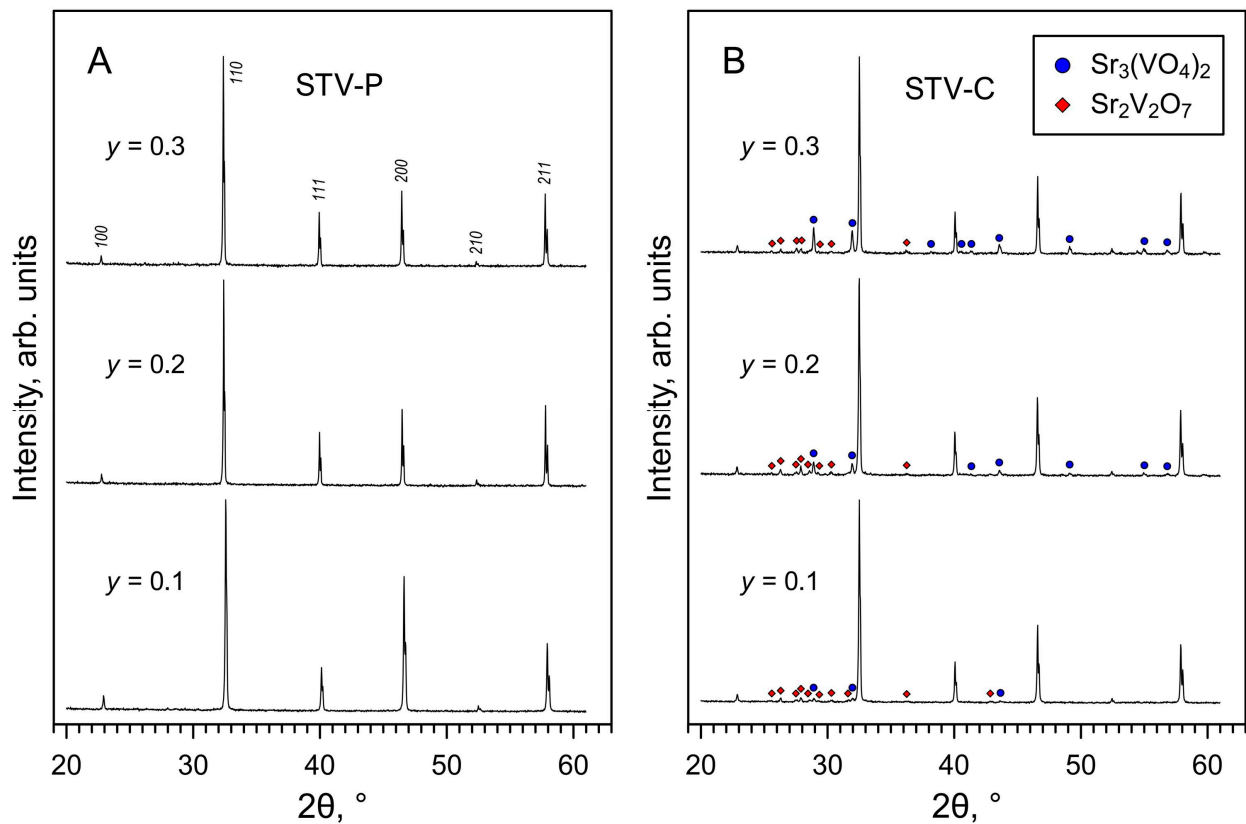


Figure 1. XRD patterns of as-prepared (A) STV-P and (B) STV-C samples. The reflections of the main perovskite phase are indexed in space group $Pm\bar{3}m$. The reflections of the $\text{Sr}_2\text{V}_2\text{O}_7$ and $\text{Sr}_3(\text{VO}_4)_2$ phases are marked according to ICDD PDF no. 01-071-1593 and 01-081-1844, respectively.

Table 1. Parameters of cubic perovskite lattice and density of as-prepared ceramic samples.

Nominal y	STV-P			STV-C
	a , Å	Density, g/cm^3	Relative Density, % ¹	Density, g/cm^3
0.1	3.9059(1)	3.20	63	2.31
0.2	3.9047(1)	3.30	64	2.38
0.3	3.9042(1)	3.29	64	2.81

¹ Theoretical density of STV-P oxides was estimated assuming nominal cation composition and neglecting possible oxygen nonstoichiometry.

Reduced $\text{SrTi}_{1-y}\text{V}_y\text{O}_{3-\delta}$ perovskites comprise vanadium cations in an average oxidation state of $\leq 4+$ with a comparatively small fraction of V^{3+} [28]. Under oxidizing conditions, vanadium tends to a pentavalent state in simple V_2O_5 oxide [24,43] as well as in pseudo-binary compounds such as $\text{Sr}_4\text{V}_2^{5+}\text{O}_9$, $\text{Sr}_3(\text{V}_2^{5+}\text{O}_4)_2$, $\text{Sr}_2\text{V}_2^{5+}\text{O}_7$ and $\text{Sr}(\text{V}^{5+}\text{O}_3)_2$ in the $\text{SrO}-\text{V}_2\text{O}_5$ system [44–46]. This is also reflected by the ready transformation of perovskite-type $\text{SrV}^{4+}\text{O}_{3-\delta}$ into $\text{Sr}_2\text{V}_2^{5+}\text{O}_7$ pyrovanadate upon thermal treatment in air [25,26]. Hence, the oxidation state of vanadium cations in oxidized $\text{SrTi}_{1-y}\text{V}_y\text{O}_{3\pm\delta}$ is expected to be not less than $4+$. It is commonly known that a close-packed cubic perovskite structure cannot accommodate interstitial oxygen ions. Taking the site conservation condition into account, the formation of oxidized $\text{SrTi}_{1-y}\text{V}_y\text{O}_{3\pm\delta}$ may occur according to one of the following two scenarios:

- (a) High-temperature treatments force the reduction of vanadium cations and their incorporation into the titanium sublattice in the V^{4+} state. This should lead to the formation of oxygen-stoichiometric perovskite.
- (b) A scenario similar to other oxidized donor-doped strontium titanates with a nominal cation stoichiometry such as $Sr_{1-x}La_xTiO_{3\pm\delta}$ or $SrTi_{1-y}Nb_yO_{3\pm\delta}$. Incorporation of a higher-valence cation into one of the sublattices, e.g., V^{5+} into the Ti^{4+} sublattice, is compensated by the formation of extended defects in the lattice—SrO shear planes characteristic of Ruddlesden-Popper phases combined with A-site cation vacancies, and/or defect clusters built of donor cations and interstitial oxygen ions [18,23,47,48].

Whatever the mechanism, the XRD results support the formation of phase-pure oxidized $SrTi_{1-y}V_yO_{3\pm\delta}$ perovskites.

In the case of the STV-C series, the XRD results showed the formation of multi-phase samples comprising at least two phases in addition to the main $SrTiO_3$ -based cubic perovskite (Figure 1B). These two phases were identified as rhombohedral strontium orthovanadate $Sr_3(VO_4)_2$ and tetragonal strontium pyrovanadate $Sr_2V_2O_7$. It is noteworthy that the latter is a low-temperature β - $Sr_2V_2O_7$ modification reported by Baglio and Dann [49]. In a previous work [26], a solid state synthesis of strontium pyrovanadate and oxidation of perovskite-type $SrVO_{3-\delta}$ in air yielded a high-temperature triclinic α - $Sr_2V_2O_7$ polymorph. Thus, the processing of STV-C samples at relatively low temperatures (compared to the STV-P series) prevented the formation of solid solutions and produced composite samples comprising strontium titanate and strontium vanadate phases. The fractions of vanadates, particularly $Sr_3(VO_4)_2$, reasonably increase with increasing vanadium content in nominal $SrTi_{1-y}V_yO_z$ (Figure 1B).

The prepared ceramics of both series were porous, as dictated by the low sintering temperatures (Figure 2). The estimations showed that the relative density of STV-P samples corresponded to 63–64% (Table 1). The grain size varied from 1.5–2.0 to 15–19 μm (Figure 2A). Changes in V content did not have a visible impact on the microstructure.

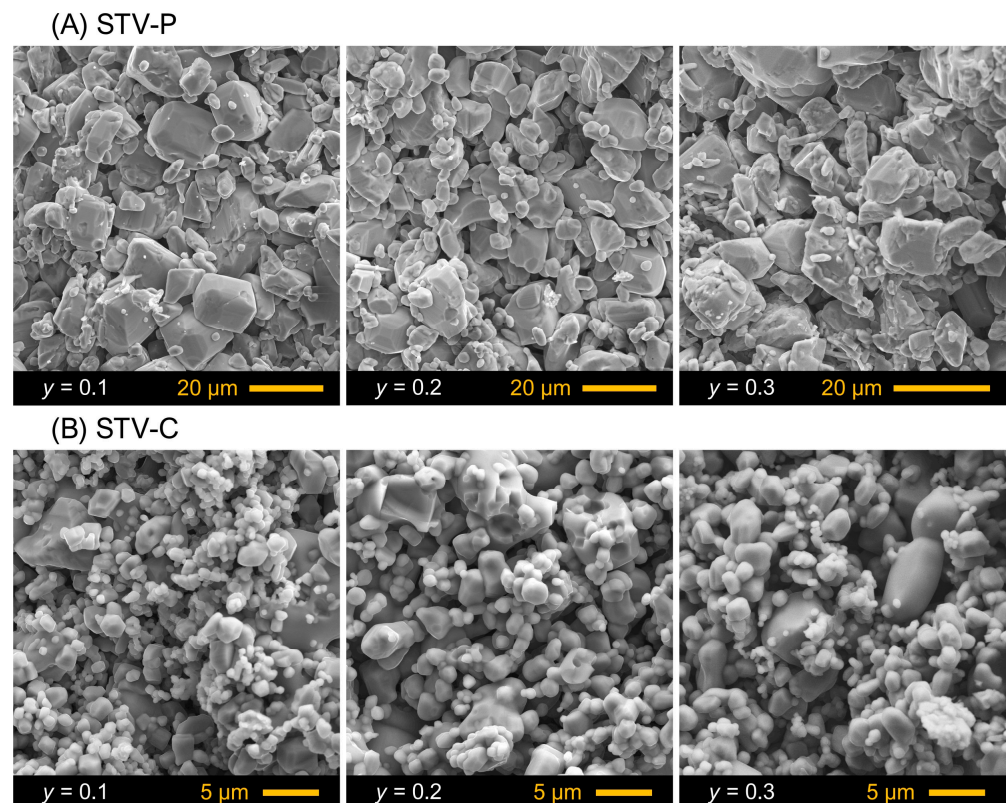


Figure 2. SEM images of fractured cross-sections of as-prepared (A) STV-P and (B) STV-C ceramics.

At the same time, EDS analysis revealed the presence of V-rich inclusions in all as-prepared STV-P samples; a representative example of an SEM/EDS image is shown in Figure 3A. These observations indicate that, in fact, STV-P samples comprised secondary phases of the Sr-V-O system undetected by the XRD, either due to a small fraction or an amorphous state. Note that the processing conditions were close to the melting point of $\text{Sr}_2\text{V}_2\text{O}_7$ pyrovanadate (1125–1160 °C [44–46]). The presence of Sr-V-O impurities also implies that the actual vanadium content in the titanium sublattice of prepared $\text{SrTi}_{1-y}\text{V}_y\text{O}_{3\pm\delta}$ perovskites is somewhat below the nominal.

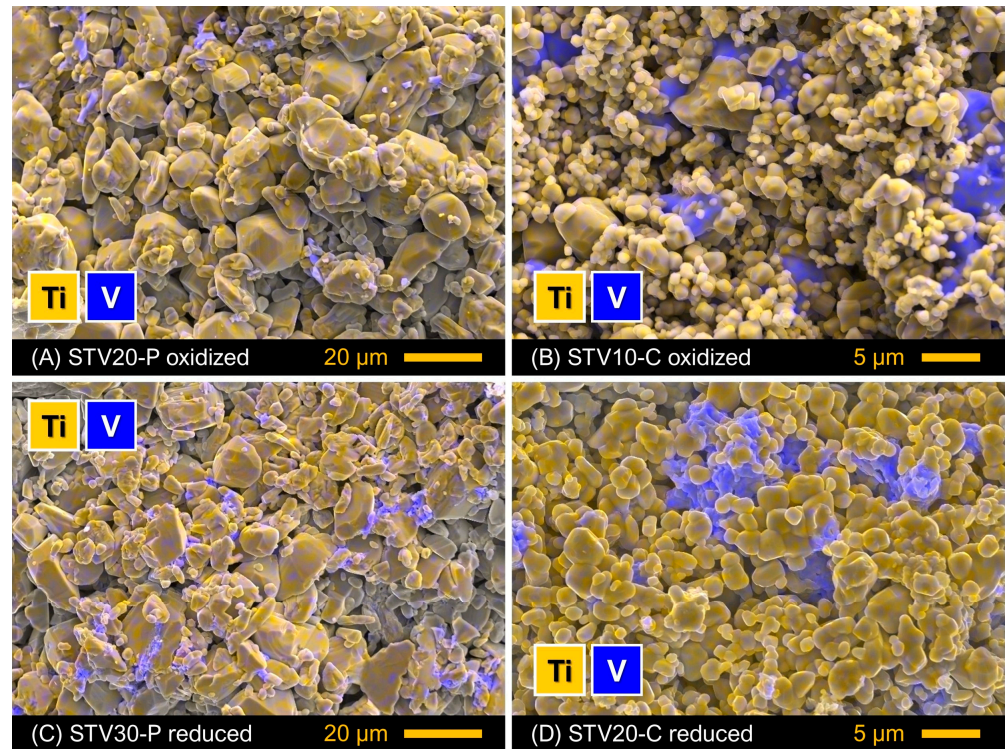


Figure 3. Examples of SEM images with overlaid EDS elemental mapping obtained from the fractured surface of (A,B) as-prepared ceramics and (C,D) reduced samples.

The lower processing temperature compared to the STV-P series resulted in a smaller average grain size of STV-C samples (Figure 2B). The size of particles varied between 0.5–1.0 and 5–7 μm . Sr-V-O components were found to exist mainly as agglomerates of 3.5–5.5 μm in size (Figure 3B). The STV-C composites had even lower densities with respect to STV-P ceramics (Table 1), which may indicate comparable or higher porosity. Note that the theoretical density of $\text{Sr}_3(\text{VO}_4)_2$ (4.47 g/cm^3) and $\beta\text{-Sr}_2\text{V}_2\text{O}_7$ (4.05 g/cm^3) (see ICDD PDF no. 01-071-1593 and 01-081-1844) is lower compared to SrTiO_3 (~5.13 g/cm^3).

3.2. Phase Changes on Reduction

Figure 4 shows the representative thermogravimetric data for powdered STV30-P and STV30-C samples recorded during the reduction in the 10% $\text{H}_2\text{-N}_2$ atmosphere. The shape of the TGA curves on heating suggests that reduction involves several processes that may include phase and structural transformations and changes in the oxidation state of vanadium cations in the perovskite-type $\text{Sr}(\text{Ti},\text{V})\text{O}_{3\pm\delta}$ lattice. The partial reduction of titanium cations may also occur to some extent, but the contribution of this process to overall weight changes is expected to be negligible.

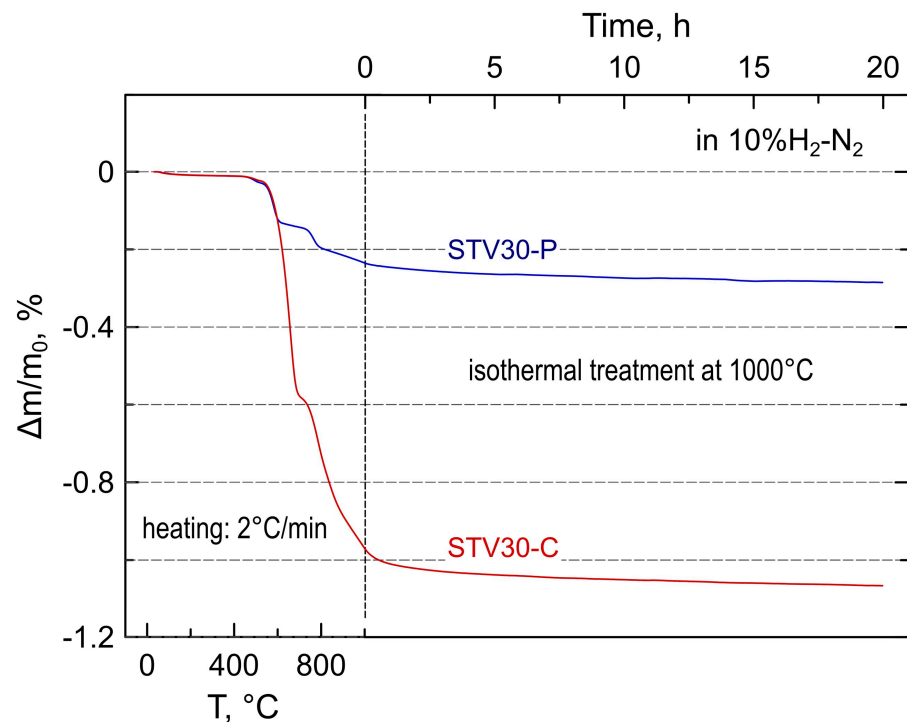


Figure 4. Relative weight loss of STV30 samples on reduction in a 10% H_2 - N_2 mixture flow. The procedure included heating at 2 $^\circ\text{C}/\text{min}$ to 1000 $^\circ\text{C}$ followed by isothermal treatment at this temperature for 20 h.

The TGA curve of the STV-C sample (Figure 4) qualitatively resembles the corresponding curve reported for $\text{Sr}_2\text{V}_2\text{O}_7$ under similar conditions, with a characteristic inflection at 690–730 $^\circ\text{C}$ [26,27]. It has been suggested that the reductive transformation of $\text{Sr}_2\text{V}_2\text{O}_7$ pyrovanadate into $\text{SrVO}_{3-\delta}$ perovskite occurs via the $5\text{Sr}_3(\text{VO}_4)_2 + \text{SrV}_6\text{O}_{11}$ intermediate, and the inflection in the thermogravimetric curve corresponds to the complete transformation of pyrovanadate into the intermediate mixture and the onset of perovskite phase [26]. While this first step occurs comparatively fast, the kinetics of the reduction of $\text{Sr}_3(\text{VO}_4)_2$ is slower, and a higher temperature and a longer time are required for the complete conversion of orthovanadate into perovskite-type $\text{SrVO}_{3-\delta}$. This is reflected by a slow drift in sample weights during the isothermal reduction step at 1000 $^\circ\text{C}$ (Figure 4).

The XRD inspections of the reduced STV-P samples revealed the presence of a small fraction of a second perovskite phase in addition to the main SrTiO_3 -based solid solution (Figure 5A). This phase was identified as perovskite-like $\text{SrVO}_{3-\delta}$. This indicates that the Sr-V-O inclusions in as-prepared STV-P samples undetected by the XRD transformed into $\text{SrVO}_{3-\delta}$ on reduction (although traces of $\text{Sr}_3(\text{VO}_4)_2$ cannot be completely excluded). The reduced STV-C samples consisted of three detectable phases: perovskite-type SrTiO_3 , $\text{SrVO}_{3-\delta}$ and unconverted $\text{Sr}_3(\text{VO}_4)_2$ orthovanadate (Figure 5B). The fraction of $\text{SrVO}_{3-\delta}$ increased with the total vanadium content, while the fraction of residual strontium orthovanadate showed the opposite trend. Reduction had no noticeable effect on the microstructure of STV-P and STV-C samples (Figure 3C,D), except that the surface of Sr-V-O agglomerates, which was smooth in oxidized samples, became etched after reduction as a result of phase transformation.

The weight changes during the reduction of the STV-C sample (Figure 4) can be assigned to a massive reduction of V^{5+} to V^{4+} or mixed $\text{V}^{4+/3+}$ state in the course of transformation of $\text{Sr}_2\text{V}_2\text{O}_7$ and $\text{Sr}_3(\text{VO}_4)_2$ into $\text{SrVO}_{3-\delta}$. Note that $\text{SrVO}_{3-\delta}$ exhibits variable oxygen nonstoichiometry under reducing conditions, which tends to $\delta \sim 0.1$ at 1000 $^\circ\text{C}$ in a 10% H_2 - N_2 atmosphere [26–28]; this corresponds to the average oxidation state of vanadium cations of $\sim 3.8+$. The weight loss during the reduction of the STV-P sample

was ~5 times lower (Figure 4). Assuming that all vanadium is in a 4+ state after heating to 1000 °C in a 10%H₂-N₂ atmosphere, rough estimations yield the average oxidation state of vanadium of ~4.18+ in the oxidized as-prepared sample. This observation implies that the formation of SrTi_{1-y}V_yO_{3±δ} perovskite under oxidizing conditions follows the first scenario (see discussion above): vanadium is forced into a 4+ state to incorporate into the titanium sublattice even under oxidizing conditions. The average oxidation state slightly higher than 4+ probably mainly originates from V⁵⁺ in the residual secondary phases. Earlier, Park et al. concluded, based on X-ray photoelectron spectroscopy results, that V⁴⁺ predominates over V⁵⁺ in SrTi_{0.8}V_{0.2}O₃ thin films prepared under an ambient atmosphere [38].

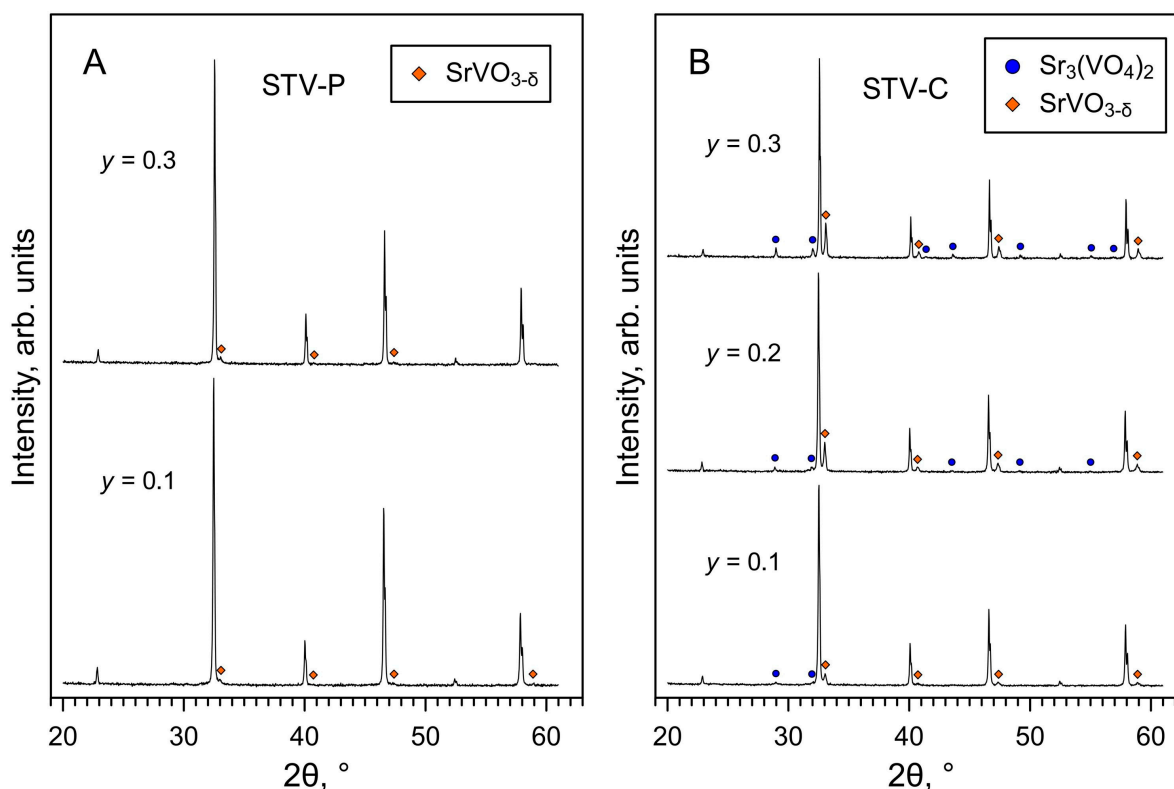


Figure 5. XRD patterns of (A) STV-P and (B) STV-C samples reduced in a 10%H₂-N₂ mixture flow at 1000 °C for 20 h. The reflections of the SrVO_{3-δ} and Sr₃(VO₄)₂ phases are marked according to ICDD PDF no. 01-081-0119 and 01-081-1844, respectively.

3.3. Thermal Expansion and Dimensional Changes

Figure 6 depicts the representative dilatometric data obtained in air and in a 10%H₂-N₂ atmosphere. Both the STV-P and STV-C samples exhibit smooth, nearly linear thermal expansion in air. The average linear thermal expansion coefficients in air vary in a narrow range of 11.1–12.1 ppm/K at 30–1000 °C (Table 2). The thermomechanical behavior of the prepared samples is defined by the properties of the SrTiO₃ perovskite phase with TEC = 11.7 ppm/K. Note that Sr₂V₂O₇ and Sr₃(VO₄)₂ ceramics were reported to exhibit slightly higher TECs in air, 15.0 and 14.3 ppm/K, respectively [26]. The TECs of STV-P and STV-C are also close to that of common solid electrolyte ceramics including yttria-stabilized zirconia, doped ceria and lanthanum gallate-based perovskites (Table 2). This ensures good thermomechanical compatibility between solid electrolytes and STV-based electrode layers.

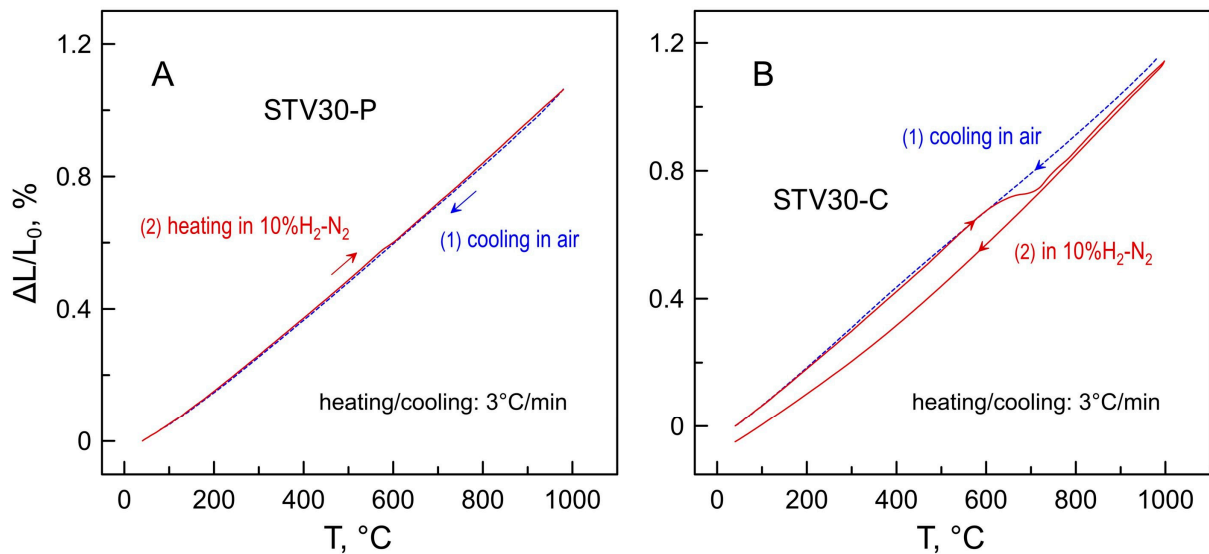


Figure 6. Dilatometric curves of (A) STV30-P and (B) STV30-C ceramic samples in air and in a 10% H_2 - N_2 atmosphere. The thermal cycle in air was followed by a cycle in reducing atmosphere.

Table 2. Average thermal expansion coefficients ($\bar{\alpha}$) calculated from the dilatometric data in air.

Composition	T Range, °C	$\bar{\alpha} \times 10^6, \text{K}^{-1}$
STV10-P	30–1000	11.2
STV20-P	30–1000	11.1
STV30-P	30–1000	11.1
STV30-C	30–1000	12.1
SrTiO_3 [16]	30–1100	11.7
8YSZ, $(\text{ZrO}_2)_{0.92}(\text{Y}_2\text{O}_3)_{0.08}$ [50]	30–1000	10.9
CGO20, $\text{Ce}_{0.8}\text{Gd}_{0.2}\text{O}_{2-\delta}$ [50]	30–1000	12.7
LSGM, $\text{La}_{0.9}\text{Sr}_{0.1}\text{Ga}_{0.8}\text{Mg}_{0.2}\text{O}_{3-\delta}$ [50]	30–1000	11.4

The dilatometric curves of oxidized STV-P samples recorded on heating in a reducing 10% H_2 - N_2 atmosphere are nearly identical to the dilatometric data obtained in air (Figure 6A). Once again, this is determined by the properties and high redox stability of the SrTiO_3 perovskite lattice. Only a minor inflection associated with the reduction process was detected in the dilatometric curves at ~ 580 – 600 °C during the first heating.

The dimensional changes caused by the reduction process were more evident in the dilatometric data of STV-C ceramic samples (Figure 6B). The inflection at 630 – 720 °C can be clearly seen in the dilatometric curve during the first heating in the reducing atmosphere. The contraction is comparatively small, $\sim 0.09\%$ in linear dimensions, and corresponds to the first step of the reductive phase transformation evidenced by the thermogravimetric analysis (Figure 4). Note that estimations based on the structural data and the results of the dilatometric experiments indicate substantial dimensional changes on redox transformations between oxidized and reduced strontium vanadates [25,26]. In particular, the comparison of unit cell volumes implies that the complete transformation of tetragonal β - $\text{Sr}_2\text{V}_2\text{O}_7$ pyrovanadate ($V_{\text{UC}} = 1276.18 \text{ \AA}^3$, $z = 8$, ICDD PDF no. 01-071-1593) into cubic $\text{SrVO}_{3-\delta}$ ($V_{\text{UC}} = 56.66 \text{ \AA}^3$, $z = 1$, ICDD PDF no. 01-081-0119) should result in volume shrinkage by $\sim 29\%$ (or $\sim 11\%$ in linear dimensions). In the case of porous STV-C samples, the fraction of $\text{Sr}_2\text{V}_2\text{O}_7$ is comparatively small, and reduction-induced dimensional changes are partly accommodated by the volume of pores. This ensures only a minor shrinkage of composite samples caused by reduction. After the first heating cycle, the reduced STV-C ceramics showed smooth moderate dimensional changes on thermal cycling in a 10% H_2 - N_2 atmosphere.

3.4. Electrical Conductivity

Figure 7 shows the data on the electrical conductivity of as-prepared materials measured in air at 750–1000 °C. All ceramics exhibit semiconducting behavior and comparatively low values of electrical conductivity, in the range $(1\text{--}4) \times 10^{-4}$ S/cm at 900 °C, partly due to the high porosity of the samples. The electrical conductivity of STV-P ceramics was essentially independent of the composition. On the contrary, the total conductivity of STV-C composites varies with nominal vanadium content and decreases in the sequence, $\sigma_{\text{STV10}} > \sigma_{\text{STV30}} > \sigma_{\text{STV20}}$. This seems to reflect an interplay between the fractions and conductivity of individual phases and the porosity of the samples. The values of the electrical conductivity of “undoped” polycrystalline SrTiO₃ ceramics reported in the literature depend on the purity and fabrication conditions and may reach 7×10^{-3} S/cm at 900 °C in air [16]. Polycrystalline Sr₂V₂O₇ and Sr₃(VO₄)₂ ceramics exhibit lower conductivity under these conditions, $\sim 4 \times 10^{-4}$ and 1×10^{-4} S/cm, respectively [26,51]. Thus, the electrical conductivity of STV-C composites initially decreases with increasing fractions of low-conducting Sr-V-O phases but then slightly increases for the STV30-C sample due to reduced porosity (as follows from the values of density, Table 1).

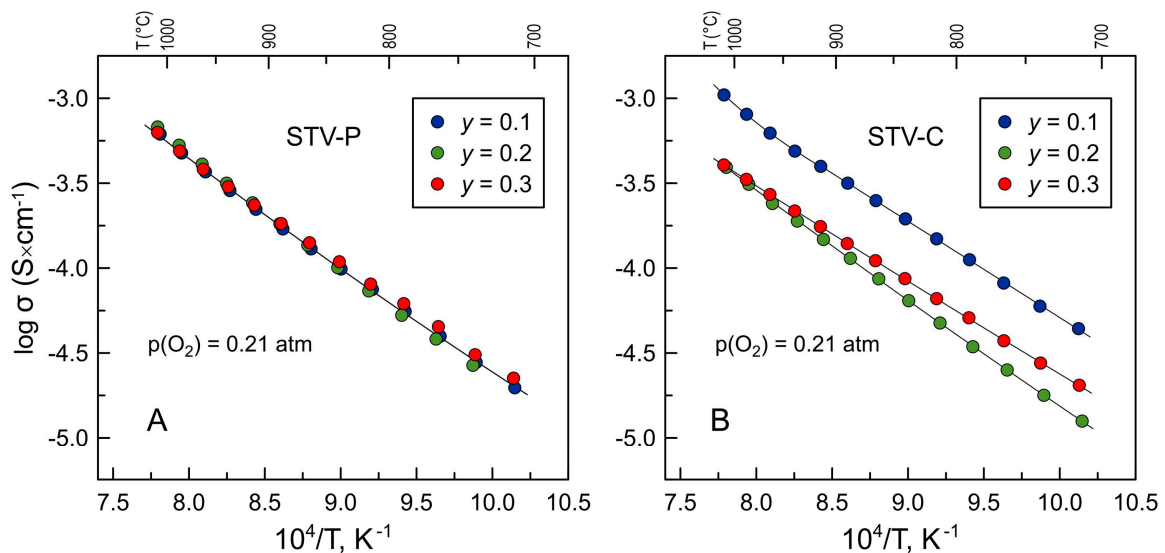
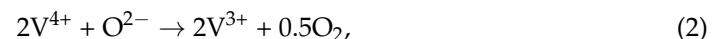
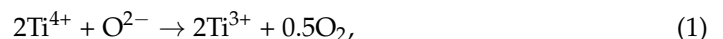


Figure 7. Total electrical conductivity of (A) STV-P and (B) STV-C ceramics in air.

The isothermal reduction in the 10%H₂-N₂ atmosphere at 900 °C results in ~ 2.5 orders of magnitude increase in the electrical conductivity of porous STV-P ceramics (Figure 8A). An increase in conductivity on reduction can be attributed to the partial reduction of titanium and vanadium cations with the generation of n-type electronic charge carriers:



where Ti³⁺ and V³⁺ are equivalent to electrons localized on titanium and vanadium cations, respectively. These equations can be rewritten as:



Electronic conductivity in the reduced STV-P perovskites is likely to occur via electron hopping between Ti⁴⁺/Ti³⁺ and V⁴⁺/V³⁺ redox pairs. The defect chemistry and electrical properties of reduced Sr(Ti,V)O_{3-δ} are discussed in detail in [28]. In addition to the increase in intrinsic electrical conductivity of the perovskite phase, the enhancement in electrical properties of STV-P samples on reduction is also likely to be partly contributed by the

transformation of residual Sr-V-O impurities into high-conducting $\text{SrVO}_{3-\delta}$ perovskite. After ~ 24 h of reduction, the conductivity reaches $(0.7\text{--}1.2) \times 10^{-1}$ S/cm and continues to grow slowly, but substantial further improvement is not expected. These values are noticeably lower compared to the conductivity of the single-phase $\text{SrTi}_{1-y}\text{V}_y\text{O}_{3-\delta}$ counterparts prepared under reducing conditions (Table 3), particularly in the case of $y = 0.2$ and 0.3 , despite comparable relative density [28].

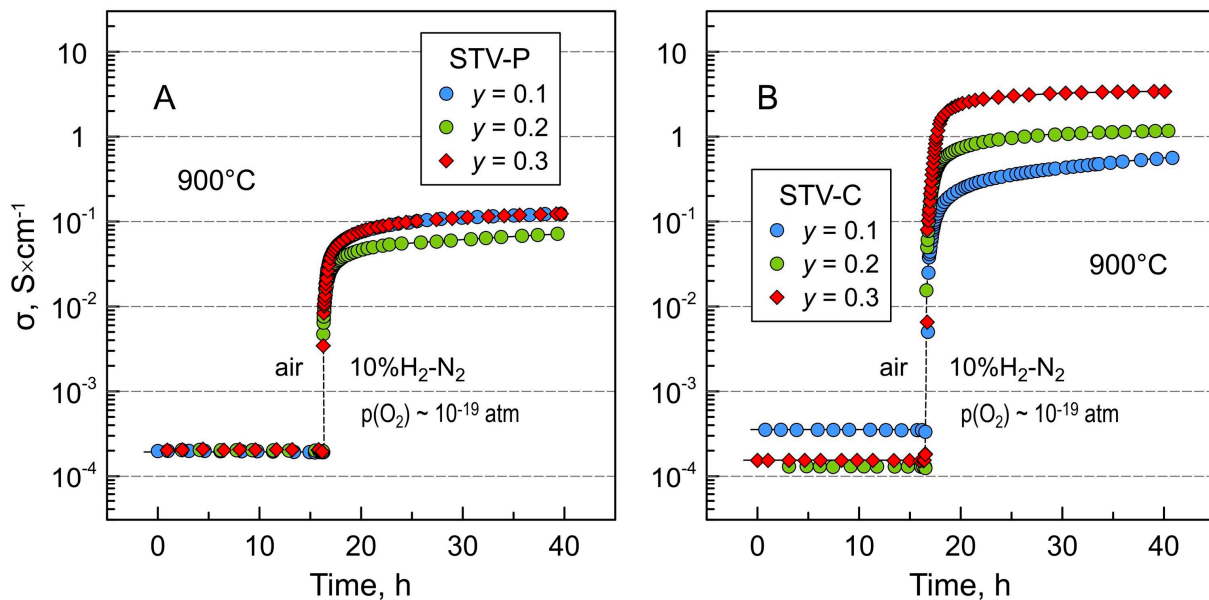


Figure 8. Relaxation of electrical conductivity of (A) STV-P and (B) STV-C ceramics on reduction at 900°C after switching from oxidizing (air) to a reducing ($10\%\text{H}_2\text{-N}_2$) atmosphere.

Table 3. Electrical conductivity of nominal $\text{SrTi}_{1-y}\text{V}_y\text{O}_z$ after reduction for 24 h in a $10\%\text{H}_2\text{-N}_2$ atmosphere at 900°C .

Nominal y	σ , S/cm (900°C , $p(\text{O}_2)\sim 10^{-20}$ atm)		
	STV-P	STV-C	$\text{SrTi}_{1-y}\text{V}_y\text{O}_{3-\delta}$ [28] ¹
0.1	0.12	0.58	0.096
0.2	0.072	1.2	0.56
0.3	0.12	3.4	3.3

¹ Single-phase perovskite ceramics synthesized and sintered under reducing conditions at 1500°C .

STV-C composite ceramics showed a more significant increase in electrical conductivity on reduction—by 3–4 orders of magnitude with respect to the level of σ under air (Figure 8B). In this case, a sharp improvement in electrical properties on reduction is associated mainly with the transformation of insulating $\text{Sr}_2\text{V}_2\text{O}_7$ and $\text{Sr}_3(\text{VO}_4)_2$ phases into $\text{SrVO}_{3-\delta}$ perovskite, which has approximately seven orders of magnitude higher conductivity at this temperature. Electrical transport in the reduced STV-C composites can be assumed to occur through percolating $\text{SrVO}_{3-\delta}$ particles and agglomerates and gradually increases with the increasing nominal vanadium content and the fraction of the $\text{SrVO}_{3-\delta}$ component (Figure 5B). Furthermore, the values of electrical conductivity of STV-C samples after reduction for ~ 24 h are similar to or even exceed the corresponding values reported for single-phase $\text{SrTi}_{1-y}\text{V}_y\text{O}_{3-\delta}$ ($y = 0.1\text{--}0.3$) perovskites (Table 3). The σ of porous reduced STV30-C reaches 3.4 S/cm, which is not optimal but may be acceptable for a solid oxide cell electrode material. In the case of the well-distributed current collection, the target conductivity for porous anode structures is set to >1 S/cm (or >10 S/cm for intrinsic material properties in a dense form) [52], although there are indications that

reasonable electrode performance can be obtained for mixed-conducting anode materials with adequate electronic conductivity of ~ 0.1 S/cm [53].

4. Conclusions

The thermal processing of precursors with nominal composition $\text{SrTi}_{1-y}\text{V}_y\text{O}_z$ ($y = 0.1, 0.2, 0.3$) at temperatures not exceeding 1100 °C yields composite ceramics comprising perovskite-type SrTiO_3 , pyrovanadate $\text{Sr}_2\text{V}_2\text{O}_7$ and orthovanadate $\text{Sr}_3(\text{VO}_4)_2$ phases. The fractions of vanadate phases increase with nominal vanadium content, and orthovanadate dominates over pyrovanadate. Increasing firing temperatures to 1250 – 1440 °C enables the formation of $\text{SrTi}_{1-y}\text{V}_y\text{O}_{3\pm\delta}$ perovskites. While the XRD results suggested that these ceramics are phase-pure, the SEM/EDS analysis revealed the co-existence of Sr-V-O precipitates, indicating that vanadium content in the perovskite lattice is lower than nominal. The results of the thermogravimetric analysis suggest that vanadium substitutes into titanium sublattice predominantly as V^{4+} even under oxidizing conditions at elevated temperatures.

Both perovskite and composite materials exhibit moderate thermal expansion coefficients in air, 11.1 – 12.1 ppm/K at 30 – 1000 °C. Reduction results in negligible dimensional changes in perovskite samples and only minor contractions of composite ceramics ($<0.1\%$ in linear dimensions during the first heating). While as-prepared porous ceramic samples exhibit low electrical conductivity in air in the order of 10^{-4} S/cm at 900 °C, reduction in $10\% \text{H}_2\text{-N}_2$ at 900 °C results in an increase in conductivity by several orders of magnitude. The electrical conductivity of perovskite samples remains comparatively low after reduction, ~ 0.1 S/cm at 900 °C. On the contrary, the transformation of oxidized vanadate phases in composite samples into high-conductive perovskite-like $\text{SrVO}_{3-\delta}$ on reduction results in substantially higher conductivity, which increases with nominal vanadium content and reaches 3.4 S/cm at 900 °C for porous ceramics with nominal $\text{SrTi}_{0.7}\text{V}_{0.3}\text{O}_z$ composition.

The processing route employing multi-component oxidized $\text{Sr}(\text{Ti},\text{V})\text{O}_z$ precursors appears to be a preferential approach enabling the preparation of composite anodes, where SrTiO_3 acts as a redox-stable structural element and the SrVO_3 phase is responsible for electrical performance. In follow-up work, further improvements are expected to be achieved through the modification of the SrTiO_3 component via donor-type doping and the optimization of the processing route and microstructure to facilitate the reduction process of oxidized precursors and attain a more uniform distribution and percolation of the SrVO_3 phase.

Author Contributions: Conceptualization, J.M., J.R.F. and A.A.Y.; methodology, J.M. and A.A.Y.; investigation and data analysis, J.M. and A.A.Y.; writing—original draft preparation, A.A.Y.; writing—review and editing, J.M., J.R.F. and A.A.Y.; supervision and funding acquisition, J.R.F. and A.A.Y. All authors have read and agreed to the published version of the manuscript.

Funding: This work was developed within the scope of the project CICECO-Aveiro Institute of Materials (UIDB/50011/2020, UIDP/50011/2020, and LA/P/0006/2020) financed by national funds through the FCT/MCTES (PIDDAC).

Institutional Review Board Statement: Not applicable.

Informed Consent Statement: Not applicable.

Data Availability Statement: Data are contained within the article and available from the corresponding author upon reasonable request.

Conflicts of Interest: The authors declare no conflict of interest.

References

1. Gong, M.; Liu, X.; Trembly, J.; Johnson, C. Sulfur-tolerant anode materials for solid oxide fuel cell application. *J. Power Sources* **2007**, *168*, 289–298. [[CrossRef](#)]
2. Zhou, X.; Yan, N.; Chuang, K.T.; Luo, J. Progress in La-doped SrTiO_3 (LST)-based anode materials for solid oxide fuel cells. *RSC Adv.* **2014**, *4*, 118–131. [[CrossRef](#)]

3. Gür, T.M. Comprehensive review of methane conversion in solid oxide fuel cells: Prospects for efficient electricity generation from natural gas. *Progr. Energy Combust. Sci.* **2016**, *54*, 1–64. [[CrossRef](#)]
4. Shu, L.; Sunarso, J.; Hashim, S.S.; Mao, J.; Zhou, W.; Liang, F. Advanced perovskite anodes for solid oxide fuel cells: A review. *Int. J. Hydrogen Energy* **2019**, *44*, 31275–31304. [[CrossRef](#)]
5. Sadykov, V.A.; Ereemeev, N.F.; Sadovskaya, E.M.; Shlyakhtina, A.V.; Pikalova, E.Y.; Osinkin, D.A.; Yaremchenko, A.A. Design of materials for solid oxide fuel cells, permselective membranes, and catalysts for biofuel transformation into syngas and hydrogen based on fundamental studies of their real structure, transport properties, and surface reactivity. *Curr. Opin. Green Sustain. Chem.* **2022**, *33*, 100558. [[CrossRef](#)]
6. Christensen, J.O.; Longo, G.; Bausinger, H.; Mai, A.; Sudireddy, B.R.; Hagen, A. Performance and sulfur tolerance of a short stack with solid oxide cells using infiltrated strontium titanate based anodes. *J. Power Sources* **2023**, *580*, 233458. [[CrossRef](#)]
7. Ettler, M.; Timmermann, H.; Malzbender, J.; Weber, A.; Menzler, N.H. Durability of Ni anodes during reoxidation cycles. *J. Power Sources* **2010**, *195*, 5452–5467. [[CrossRef](#)]
8. Iwanschitz, B.; Holzer, L.; Mai, A.; Schütze, M. Nickel agglomeration in solid oxide fuel cells: The influence of temperature. *Solid State Ion.* **2012**, *211*, 69–73. [[CrossRef](#)]
9. Kan, W.H.; Thangadurai, V. Challenges and prospects of anodes for solid oxide fuel cells (SOFCs). *Ionics* **2015**, *21*, 301–318. [[CrossRef](#)]
10. Kurokawa, H.; Yang, L.; Jacobson, C.P.; De Jonghe, L.C.; Visco, S.J. Y-doped SrTiO₃ based sulfur tolerant anode for solid oxide fuel cells. *J. Power Sources* **2007**, *164*, 510–518. [[CrossRef](#)]
11. Tamm, K.; Küngas, R.; Gorte, R.J.; Lust, E. Solid oxide fuel cell anodes prepared by infiltration of strontium doped lanthanum vanadate into doped ceria electrolyte. *Electrochim. Acta* **2013**, *106*, 398–405. [[CrossRef](#)]
12. Niu, B.; Jin, F.; Fu, R.; Feng, T.; Shen, Y.; Liu, J.; He, T. Pd-impregnated Sr_{1.9}VMoO_{6-δ} double perovskite as an efficient and stable anode for solid-oxide fuel cells operating on sulfur-containing syngas. *Electrochim. Acta* **2018**, *274*, 91–102. [[CrossRef](#)]
13. Shao, L.; Si, F.; Fu, X.Z.; Luo, J.L. Archiving high-performance solid oxide fuel cells with titanate anode in sulfur- and carbon-containing fuels. *Electrochim. Acta* **2018**, *280*, 9–13. [[CrossRef](#)]
14. Niu, B.; Jin, F.; Liu, J.; Zhang, Y.; Jiang, P.; Feng, T.; Xu, B.; He, T. Highly carbon- and sulfur-tolerant Sr₂TiMoO_{6-δ} double perovskite anode for solid oxide fuel cells. *Int. J. Hydrogen Energy* **2019**, *44*, 20404–20415. [[CrossRef](#)]
15. Cai, W.; Cao, D.; Zhou, M.; Yan, X.; Li, Y.; Wu, Z.; Lü, S.; Mao, C.; Xie, Y.; Zhao, C.; et al. Sulfur-tolerant Fe-doped La_{0.3}Sr_{0.7}TiO₃ perovskite as anode of direct carbon solid oxide fuel cells. *Energy* **2020**, *211*, 118958. [[CrossRef](#)]
16. Yaremchenko, A.A.; Macías, J.; Kovalevsky, A.V.; Arias-Serrano, B.I.; Frade, J.R. Electrical conductivity and thermal expansion of Ln-substituted SrTiO₃ for solid oxide cell electrodes and interconnects: The effect of rare-earth cation size. *J. Power Sources* **2020**, *474*, 228531. [[CrossRef](#)]
17. Slater, P.R.; Fagg, D.P.; Irvine, J.T.S. Synthesis and electrical characterisation of doped perovskite titanates as potential anode materials for solid oxide fuel cells. *J. Mater. Chem.* **1997**, *7*, 2495–2498. [[CrossRef](#)]
18. Marina, O.A.; Canfield, N.L.; Stevenson, J.W. Thermal, electrical, and electrocatalytic properties of lanthanum-doped strontium titanate. *Solid State Ion.* **2002**, *149*, 21–28. [[CrossRef](#)]
19. Hashimoto, S.; Kindermann, L.; Poulsen, F.W.; Mogensen, M. A study on the structural and electrical properties of lanthanum-doped strontium titanate prepared in air. *J. Alloys Compd.* **2005**, *397*, 245–249. [[CrossRef](#)]
20. Łącz, A.; Drożdż, E. Porous Y and Cr-doped SrTiO₃ materials—Electrical and redox properties. *J. Solid State Electrochem.* **2019**, *23*, 2989–2997. [[CrossRef](#)]
21. Hashimoto, S.; Poulsen, F.W.; Mogensen, M. Conductivity of SrTiO₃ based oxides in the reducing atmosphere at high temperature. *J. Alloys Compd.* **2007**, *439*, 232–236. [[CrossRef](#)]
22. Neagu, D.; Irvine, J.T.S. Structure and properties of La_{0.4}Sr_{0.4}TiO₃ ceramics for use as anode materials in solid oxide fuel cells. *Chem. Mater.* **2010**, *22*, 5042–5053. [[CrossRef](#)]
23. Yaremchenko, A.A.; Naumovich, E.N.; Patrício, S.G.; Merkulov, O.V.; Patrakeevev, M.V.; Frade, J.R. Rare-earth—substituted strontium titanate: Insight into local oxygen-rich structures and redox kinetics. *Inorg. Chem.* **2016**, *55*, 4836–4849. [[CrossRef](#)] [[PubMed](#)]
24. Hui, S.; Petric, A. Conductivity and stability of SrVO₃ and mixed perovskites at low oxygen partial pressures. *Solid State Ionics* **2001**, *143*, 275–283. [[CrossRef](#)]
25. Cheng, Z.; Zha, S.; Aguilar, L.; Liu, M. Chemical, electrical, and thermal properties of strontium doped lanthanum vanadate. *Solid State Ion.* **2005**, *176*, 1921–1928. [[CrossRef](#)]
26. Macías, J.; Yaremchenko, A.A.; Frade, J.R. Redox transitions in strontium vanadates: Electrical conductivity and dimensional changes. *J. Alloys Compd.* **2014**, *601*, 186–194. [[CrossRef](#)]
27. Rey, M.J.; Dehaut, P.; Joubert, J.C.; Lambert-Andron, B.; Cyrot, M.; Cyrot-Lackmann, F. Preparation and structure of the compounds SrVO₃ and Sr₂VO₄. *J. Solid State Chem.* **1990**, *86*, 101–108. [[CrossRef](#)]
28. Macías, J.; Yaremchenko, A.A.; Rodríguez-Castellón, E.; Sarykevich, M.; Frade, J.R. Compromising between phase stability and electrical performance: SrVO₃-SrTiO₃ solid solutions as solid oxide fuel cell anode components. *ChemSusChem* **2019**, *12*, 240–251. [[CrossRef](#)]
29. Macías, J.; Yaremchenko, A.A.; Frade, J.R. Enhanced stability of perovskite-like SrVO₃-based anode materials by donor-type substitutions. *J. Mater. Chem. A* **2016**, *4*, 10186–10194. [[CrossRef](#)]

30. Macías, J.; Yaremchenko, A.A.; Fagg, D.P.; Frade, J.R. Structural and defect chemistry guidelines for Sr(V,Nb)O₃-based SOFC anode materials. *Phys. Chem. Chem. Phys.* **2015**, *17*, 10749–10758. [CrossRef]
31. Tsuiki, H.; Kitazawa, K.; Fueki, K. The donor level of V⁴⁺ and the metal-nonmetal transition in SrTi_{1-x}V_xO₃. *Jpn. J. Appl. Phys.* **1983**, *22*, 590–596. [CrossRef]
32. Hong, K.; Kim, S.H.; Heo, Y.J.; Kwon, Y.U. Metal-insulator transitions of SrTi_{1-x}V_xO₃ solid solution system. *Solid State Commun.* **2002**, *123*, 305–310. [CrossRef]
33. Seródio Costa, B.F.; Arias-Serrano, B.I.; Yaremchenko, A.A. Development of Ni-Sr(V,Ti)O_{3-δ} fuel electrodes for solid oxide fuel cells. *Materials* **2022**, *15*, 278. [CrossRef] [PubMed]
34. Wang, J.; Li, H.; Li, H.; Yin, S.; Sato, T. Visible-light induced photocatalytic activity of vanadium and nitrogen co-doped SrTiO₃. *Solid State Phenom.* **2009**, *147–149*, 851–855. [CrossRef]
35. Hoang, V.Q.T.; Phan, T.Q.P.; Senthilkumar, V.; Doan, V.T.; Kim, Y.S.; Le, M.V. Enhanced photocatalytic activities of vanadium and molybdenum co-doped strontium titanate under visible light. *Int. J. Appl. Ceram. Technol.* **2019**, *16*, 1651–1658. [CrossRef]
36. Deng, C.; Zeng, Y.; Zhao, J.; Wang, C. Effect of doping vanadium on optical and photocatalytic properties of SrTiO₃. *Acta Mater. Compos. Sin.* **2019**, *36*, 2950–2958. [CrossRef]
37. Bantawal, H.; Shenoy, U.S.; Bhat, D.K. Vanadium-doped SrTiO₃ nanocubes: Insight into role of vanadium in improving the photocatalytic activity. *Appl. Surf. Sci.* **2020**, *513*, 145858. [CrossRef]
38. Park, C.S.; Hong, M.H.; Cho, H.H.; Park, H.H. Enhancement of Seebeck coefficient of mesoporous SrTiO₃ with V-group elements V, Nb, and Ta substituted for Ti. *J. Eur. Ceram. Soc.* **2018**, *38*, 125–130. [CrossRef]
39. Mantry, S.P.; Yadav, A.; Fahad, M.; Sarun, P.M. Effect of vanadium substitution on the dielectric and electrical conduction properties of SrTiO₃ ceramics. *Mater. Res. Express* **2018**, *5*, 036303. [CrossRef]
40. Elcogen Solid Oxide Fuel Cell User Manual (Version 2.2021, Updated 29 October 2021). Available online: <https://elcogen.com/wp-content/uploads/2022/10/Elcogen-User-Manual-2910202170-1.pdf> (accessed on 10 December 2023).
41. Kupecki, J.; Niemczyk, A.; Jagielski, S.; Kluczowski, R.; Kosiorek, M.; Machaj, K. Boosting solid oxide electrolyzer performance by fine tuning the microstructure of electrodes—Preliminary study. *Int. J. Hydrogen Energy* **2023**, *48*, 26436–26445. [CrossRef]
42. Shannon, R.D. Revised effective ionic radii and systematic studies of interatomic distances in halides and chalcogenides. *Acta Crystallogr. A* **1976**, *32*, 751–767. [CrossRef]
43. Yamaguchi, I.; Manabe, T.; Tsuchiya, T.; Nakajima, T.; Sohma, M.; Kumagai, T. Preparation and characterization of epitaxial VO₂ films on sapphire using postepitaxial topotaxy route via epitaxial V₂O₃ films. *Jpn. J. Appl. Phys.* **2008**, *47*, 1022–1027. [CrossRef]
44. Brown, J.J., Jr. Phase equilibria in the system SrO-CdO-V₂O₅. *J. Am. Ceram. Soc.* **1972**, *55*, 500–503. [CrossRef]
45. Krasnenko, T.I.; Tugova, N.P.; Slobodin, B.V.; Fotiev, A.A.; Syrneva, O.N.; Kiyayeva, G.A. Phase composition and sequence of transformations in SrO-V₂O₅ system. *Depos. Doc. VINITI* **1983**, *2866–2883*, 1–12.
46. Fotiev, A.A.; Slobodin, B.V.; Khodos, M.Y.; Pletnev, R.N. *Vanadates. Composition, Synthesis, Structure, Properties*; Nauka: Moscow, Russia, 1988.
47. Flandermeyer, B.F.; Agarwal, A.K.; Anderson, H.U.; Nasrallah, M.M. Oxidation-reduction behaviour of La-doped SrTiO₃. *J. Mater. Sci.* **1984**, *19*, 2593–2598. [CrossRef]
48. Moos, R.; Härdtl, K.H. Defect chemistry of donor-doped and undoped strontium titanate ceramics between 1000° and 1400 °C. *J. Am. Ceram. Soc.* **1997**, *80*, 2549–2562. [CrossRef]
49. Baglio, J.A.; Dann, J.N. The crystal structure of beta strontium pyrovanadate. *J. Solid State Chem.* **1972**, *4*, 87–93. [CrossRef]
50. Tietz, F. Thermal Expansion of SOFC Materials. *Ionics* **1999**, *5*, 129–139. [CrossRef]
51. Krasnenko, T.I.; Petrov, V.S.; Kudrina, L.V.; Andrianova, L.V.; Fotiev, A.A. Electrical conductivity polytherms, vaporization rate and unit cell constants of Sr and Cd pyrovanadates. *Inorg. Mater.* **1991**, *27*, 1271–1273.
52. Atkinson, A.; Barnett, S.; Gorte, R.J.; Irvine, J.T.S.; McEvoy, A.J.; Mogensen, M.; Singhal, S.C.; Vohs, J. Advanced anodes for high temperature fuel cells. *Nat. Mater.* **2004**, *3*, 17–27. [CrossRef]
53. Duranti, L.; Luisetto, I.; Licocchia, S.; Del Gaudio, C.; Di Bartolomeo, E. Electrochemical performance and stability of LSF_{Mn}+NiSDC anode in dry methane. *Electrochim. Acta* **2020**, *362*, 137116. [CrossRef]

Disclaimer/Publisher's Note: The statements, opinions and data contained in all publications are solely those of the individual author(s) and contributor(s) and not of MDPI and/or the editor(s). MDPI and/or the editor(s) disclaim responsibility for any injury to people or property resulting from any ideas, methods, instructions or products referred to in the content.